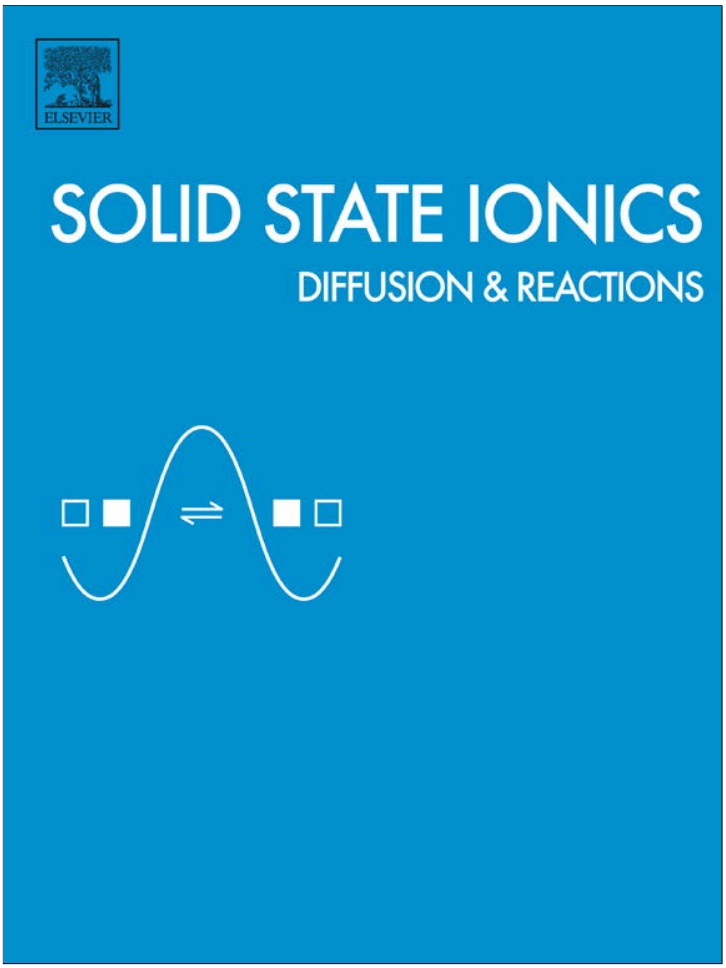

(This is a sample cover image for this issue. The actual cover is not yet available at this time.)

Solid State Ionics 233 (2013) 95–101

Contents lists available at SciVerse ScienceDirect

Solid State Ionics

journal homepage: www.elsevier.com/locate/ssi

A new crystalline LiPON electrolyte: Synthesis, properties, and electronic structure

Keerthi Senevirathne [a,d], Cynthia S. Day [a,d], Michael D. Gross [b,d], Abdessadek Lachgar [a,d,*], N.A.W. Holzwarth [c,d,**]

[a] Department of Chemistry, Wake Forest University, Winston-Salem, NC 27109, USA
[b] Department of Chemical Engineering, Bucknell University, Lewisburg, PA 17837, USA
[c] Department of Physics, Wake Forest University, Winston-Salem, NC 27109, USA
[d] Center of Energy, Environment, and Sustainability, Wake Forest University, Winston-Salem, NC 27109, USA

ARTICLE INFO

Article history:
Received 9 November 2012
Received in revised form 7 December 2012
Accepted 26 December 2012
Available online xxxx

Keywords:
Solid state synthesis
Solid electrolyte
LiPON
Lithium ion battery
Computational prediction
X-ray diffraction

ABSTRACT

The new crystalline compound, Li_2PO_2N, was synthesized using high temperature solid state methods starting with a stoichiometric mixture of Li_2O, P_2O_5, and P_3N_5. Its crystal structure was determined *ab initio* from powder X-ray diffraction. The compound crystallizes in the orthorhombic space group $Cmc2_1$ (# 36) with lattice constants $a = 9.0692(4)$ Å, $b = 5.3999(2)$ Å, and $c = 4.6856(2)$ Å. The crystal structure of *SD*-Li_2PO_2N consists of parallel arrangements of anionic chains formed of corner sharing (PO_2N_2) tetrahedra. The chains are held together by Li^+ cations. The structure of the synthesized material is similar to that predicted by Du and Holzwarth on the basis of first principles calculations (*Phys. Rev. B* **81**, 184106 (2010)). The compound is chemically and structurally stable in air up to 600 °C and in vacuum up to 1050 °C. The Arrhenius activation energy of *SD*-Li_2PO_2N in pressed pellet form was determined from electrochemical impedance spectroscopy measurements to be 0.6 eV, comparable to that of the glassy electrolyte LiPON developed at Oak Ridge National Laboratory. The minimum activation energies for Li ion vacancy and interstitial migrations are computed to be 0.4 eV and 0.8 eV, respectively. First principles calculations estimate the band gap of *SD*-Li_2PO_2N to be larger than 6 eV.

1. Introduction

Lithium phosphorous oxy-nitride "LiPON" electrolytes with the composition $Li_xPO_yN_z$, where $x = 2y + 3z - 5$, were pioneered at Oak Ridge National laboratory [1–9]. These compounds were physically deposited as amorphous thin film electrolytes for use in all solid state micro-batteries. In the course of a computational study of the broad class of crystalline lithium phosphorus oxy-nitride materials, Du and Holzwarth [10] recently predicted a stable crystalline material with the stoichiometry Li_2PO_2N. The predicted material was computationally derived from the known crystal structure [11] of $LiPO_3$ by using the following modification of the phosphate chains. Each oxygen in a bridging site between two phosphorus ions was replaced with nitrogen and one lithium was added to the chemical composition to maintain electroneutrality. The computational study showed that placing N rather than O at the bridging sites leads to the stabilization of a planar structure of the P–N–P–N backbone along the chains, consistent with an electronic configuration on the N site with sp^2 hybridization, compared with the twisted P–O–P–O backbone along the phosphate chains found in $LiPO_3$.

Various strategies have been explored to achieve stable LiPON materials, with reasonably high ionic conductivity and crystallinity, by employing diverse synthetic methods. However, most of the synthesis methods, with a few exceptions, have not produced crystalline phases of LiPON. The Oak Ridge group showed that a solid state reaction using stoichiometric amounts of Li_3N and $LiPO_3$ under N_2 atmosphere produces microcrystalline $Li_{2.88}PO_{3.73}N_{0.17}$ at relatively low temperature [4]. The ionic conductivity of this material was found to be 1×10^{-13} S/cm, which is significantly larger than the structurally similar pure lithium phosphate (γ-Li_3PO_4) but too small for electrolyte applications. By contrast, commercial LiPON thin films with ionic conductivities of typically 2×10^{-6} S/cm at 25 °C are prepared by deposition of material from radio frequency magnetron sputtering of ceramic Li_3PO_4 targets using nitrogen in the process gas [1,9].

The present paper reports the experimental preparation of the computationally predicted compound, Li_2PO_2N. Furthermore, its crystal structure determined *ab initio* from powder X-ray diffraction data was found to be similar to the two low-energy structures s_1 and s_2 found in the original optimization studies [10]. For ease of comparison with these previously predicted structures, we refer to the experimental obtained compound as *SD*-Li_2PO_2N. Computer optimization studies of the *SD* structure find it to stabilize at an energy lower by 0.1 eV/Li_2PO_2N compared to the energies of the s_1 and s_2 structures. The combination of experimental and computational studies of Li_2PO_2N reveal an interesting material composed of anionic flat chains of phosphorus oxy-nitride corner-shared tetrahedra, held together by Li^+ cations.

* Correspondence to: A. Lachgar, Department of Chemistry, Wake Forest University, Winston-Salem, NC 27109, USA.
** Correspondence to: N. A. W. Holzwarth, Department of Physics, Wake Forest University, Winston-Salem, NC 27109, USA. Tel.: +1 336 758 5510.
E-mail addresses: lachgar@wfu.edu (A. Lachgar), natalie@wfu.edu (N.A.W. Holzwarth).

0167-2738/$ – see front matter © 2013 Elsevier B.V. All rights reserved.
http://dx.doi.org/10.1016/j.ssi.2012.12.013

The structure of *SD*-Li_2PO_2N is similar to that of lithium metasilicate Li_2SiO_3 [12].

2. Methods

2.1. Synthesis methods

SD-Li_2PO_2N was synthesized using the chemical reaction

$$Li_2O(s) + \frac{1}{5}P_2O_5(s) + \frac{1}{5}P_3N_5(s) \rightarrow Li_2PO_2N(s).$$

The precursor materials, lithium oxide (Li_2O, 99.5% purity, Alfa Aesar), phosphorous pentoxide (P_2O_5, 99.99% purity, Sigma-Aldrich), and triphosphorous pentanitride (P_3N_5), received as a gift from Tianyu Chemical Co., Ltd. Zhejiang, China (>99% purity with Mn ≤ 0.001%, Mg ≤ 0.005%, Cu ≤ 0.0001%, Fe ≤ 0.001%, and Si ≤ 0.01%), were weighed in an argon filled glove box in the molar ratio of 1:0.2:0.3 and ground for approximately 15 min to form a homogenous mixture. Then, 0.25 g of the powder was pressed into a cylindrical pellet using a hand-held pellet press and placed in a quartz tube. The quartz tube fitted with a glass adaptor to prevent exposure to air was connected to a high vacuum line for 45 min prior to sealing under vacuum. Sealed tubes were heated at 950 °C for 10 h with a heating and cooling rate of 5 °C/min. The gray microcrystalline product was ground using mortar and pestle prior to further characterizations.

2.2. Analysis methods

2.2.1. X-ray analysis

A Bruker-AXS D2 Phaser Powder diffractometer (XRD) equipped with a Ni-filtered Cu K_α sealed X-ray tube ($\lambda = 1.54184$ Å) and a Lynxeye position-sensitive detector was used for X-ray analysis. The X-ray powder diffraction pattern was measured at room temperature and analyzed using the Bruker-AXS EVA software package [13]. The Bruker-AXS TOPAS software package [14] was used to index the unit cell and for the *ab initio* structure determination and Rietveld refinement.

2.2.2. Transmission electron microscopy

Electron microscopy was used to characterize morphology and crystallinity of the *SD*-Li_2PO_2N, using a JEOL 1200 EX field-emission transmission electron microscope operating at 100 kV. In the preparation of specimens, appropriate amount of powder was dispersed in ethanol by sonication for ~5 min. A drop of the resultant solution was placed on a carbon coated copper grid and allowed to dry at room temperature.

2.2.3. Thermal analysis

A Perkin Elmer Pyris 1 thermogravimetric analyzer was used to determine the relative weight loss or gain. As-prepared *SD*-Li_2PO_2N sample was heated up to 1000 °C with a temperature ramp of 2 °C min^{-1} in a flow of air. The percent weight gain was calculated relative to the initial weight of the sample.

2.2.4. Infrared spectroscopy

A PerkinElmer Spectrum 100 FTIR spectrometer was used to probe bond vibrations of *SD*-Li_2PO_2N. A ground powder of *SD*-Li_2PO_2N was directly placed on the IR holder and pressed with inbuilt press. The IR spectrum was acquired in the 650–4000 cm^{-1} range.

2.2.5. Impedance measurements

Bulk Li_2PO_2N cylindrical pellets with a thickness of 0.21 cm and a diameter of 0.65 cm were prepared by sintering pressed Li_2PO_2N powder in vacuum for 10 h. Sintering at 500 °C and 950 °C resulted in pellets with 55% and 78% of the theoretical density, respectively. Ionic conductivity values were determined with electrochemical impedance spectroscopy measurements. Silver ink and silver wires were attached to the Li_2PO_2N pellets, serving as ion-blocking electrodes. Impedance spectra were collected in an Ar atmosphere with a Gamry Instruments Series G750 potentiostat with four probes in the potentiostatic mode. The applied voltage and ac perturbation were 0 V and 1 V, respectively, over a frequency range of 0.1 Hz–300 kHz. The resistance value, used to calculate ionic conductivity as a function of temperature, was the real component of the impedance spectrum at which the imaginary component went through a local minimum.

2.3. Computer simulation methods

The computational methods are based on density functional theory [15,16]. The calculations were carried out using the Quantum Espresso (pwscf) [17] and abinit [18] packages as well as the pwpaw program [19] using the projector augmented wave (PAW) [20] formalism. The PAW basis and projector functions were generated by the atompaw

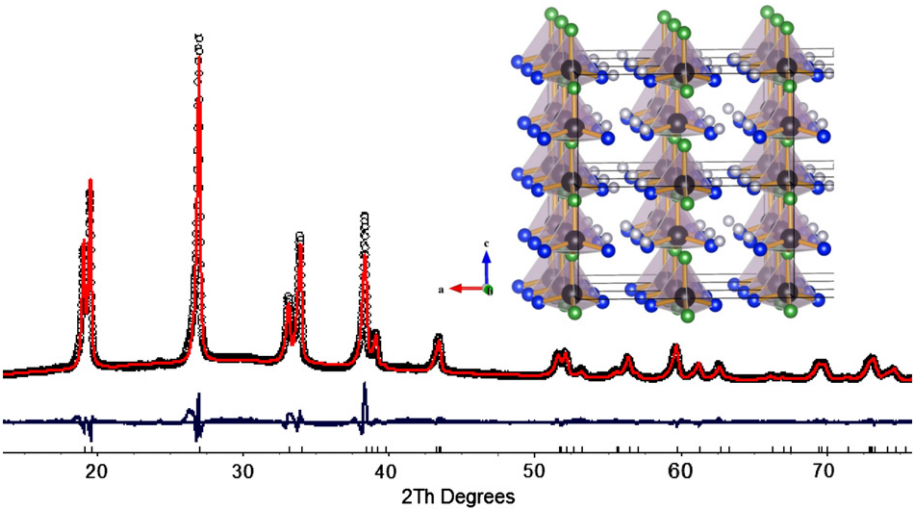

Fig. 1. X-ray crystal structure solution of *SD*-Li_2PO_2N resulting from the *ab initio* simulated annealing fit and Rietveld refinement of the XRD data using TOPAS. The observed (black dots), calculated (solid red) and difference (gray) XRD patterns are shown along with vertical bars representing the calculated Bragg reflection positions. The inset shows a visualization of the final refined structure, viewed along the b-axis, with gray, black, blue, and green spheres representing the Li, P, O, and N sites, respectively. (For interpretation of the references to color in this figure legend, the reader is referred to the web version of this article.)

Table 1
Lattice parameters and fractional coordinates (*x*,*y*,*z*) based on the conventional unit cell for *SD*-Li_2PO_2N, comparing experiment (determined from refinement of powder X-ray diffraction data) and computation (determined from optimization using the pwscf [17] code).

Experimental results[a]				Computational results		
$a=9.0692(4)$ Å, $b=5.3999(2)$ Å, $c=4.6856(2)$ Å				$a=8.86$ Å, $b=5.30$ Å, $c=4.64$ Å		
Atom	*x*	*y*	*z*	*X*	*y*	*z*
Li (8b)	0.3281(7)	0.362(2)	0.983(5)	0.333	0.341	1.002
P (4a)	0.0000	0.3414(3)	0.0000	0.000	0.343	0.000
O (8b)	0.3518(3)	0.6914(5)	0.919(1)	0.359	0.691	0.916
N (4a)	0.0000	0.631(1)	0.854(2)	0.000	0.616	0.845

[a] Space group = $Cmc2_1$ (#36), $V=229.47$ Å^3, $R_p=5.53$, $R_{wp}=7.05$, $R_{Bragg}=2.407$, and GOF = 4.55.

[21] code. The exchange-correlation functional was the local density approximation [22] (LDA). Visualizations were constructed using the OpenDX [23], XCrySDEN [24], and VESTA [25] software packages.

The calculations were performed with plane wave expansions of the wave function including $|k+G|^2 \leq 64$ bohr^{-2}. The integrals over the Brillouin zone were approximated using a Monkhorst–Pack [26] k-point sampling of $8\times8\times8$.

3. Results and discussion

3.1. Synthesis details and material properties

A high temperature solid state reaction method was employed to make *SD*-Li_2PO_2N. All manipulations were done inside an argon filled glove box. Although the precursors are not air-sensitive, it is important to handle them, especially the highly hygroscopic P_2O_5, under moisture free conditions. Approximately 90% yield relative to initial weight of the precursor mixture was recovered after the completion of the reaction. It was our experience that a slight excess of the P_3N_5 precursor was needed to obtain the single phase product. Otherwise, the product was found to be a mixture of *SD*-Li_2PO_2N and γ-Li_3PO_4, as confirmed by the powder X-ray diffraction pattern.

3.2. Structural analysis

Fig. 1 shows the X-ray data for a sample of *SD*-Li_2PO_2N prepared by the solid state reaction at 950 °C. The observed peaks for the as-prepared *SD*-Li_2PO_2N are sharp, which is indicative of high crystallinity. Powder X-ray diffraction analysis was used to determine detailed structural information and approximate crystallite size. Profile fitting methods in the Bruker-AXS TOPAS software [14] were used to generate accurate peak positions and the first 28 (major) peaks used to determine lattice parameters. Preliminary indexing results were consistent with an orthorhombic C-centered lattice with $a=9.078$ Å, $b=5.398$ Å, $c=4.686$ Å, $V=229.6$ Å^3, and GOF = 8.98. An initial analysis of the systematic absences in the powder pattern indicated space group $Cmc2_1$, (#36) [27] as a likely candidate. This choice was further supported by the success of the structure solution by *ab initio* simulated annealing methods and by subsequent Rietveld structural refinement. During the final Rietveld refinements using the $Cmc2_1$ space group, the background signal was modeled as a polynomial function. Peak shapes were described utilizing fundamental parameters and the final Rietveld refinement plots are shown in Fig. 1. Crystal data and refinement details are summarized along with lattice constants and fractional atomic coordinates for Li_2PO_2N in Table 1. Selected bond lengths and angles are provided in the supporting information (Table S1).

The *SD*-Li_2PO_2N structure is composed of Li^+ ions and planar P–N–P–N chains (with neighboring dihedral angles 0° and 180°) formed by PO_2N_2 tetrahedra linked to each other by the N atoms. The tetrahedrally-coordinated P and N atoms occupy the 4a sites in the crystallographic mirror plane (at $x=0$ or 1/2 in the unit cell). In addition to the 2 P–N bonds (1.665(7) Å and 1.708(6) Å), the P coordination environment includes 2 mirror-related oxygen atoms (O1) at a distance of P–O = 1.615(3) Å. The bond angles subtended at the phosphorous atom range from 106.2(3)° to 112.7(2)° with a 108.5(3)° angle at the phosphorous along the N–P–N chain. The nitrogen atom tetrahedral coordination is completed by two Li^+ ions with N–Li = 2.08(1) Å and the angles at nitrogen range from 96.7(6)° to 118.7(4)° (P–N–P backbone angle). The Li^+ ions are tetrahedrally-coordinated with three of the vertices occupied by oxygen atoms (1.816(10) Å, 1.898(8) Å and 2.08(2) Å) and a single nitrogen atom at 2.08(1) Å. A survey of values reported in the Cambridge Crystallographic Database [28] for similar tetrahedrally-coordinated Li^+ ions in an O_3N environment revealed mean values of 2.070 Å and 2.120 Å for Li–O and Li–N bonds, respectively. The next closest contact in the Li coordination sphere is an oxygen at 2.67(2) Å. These values are in good agreement with those previously reported for Li_2SiO_3 where the Li-oxygen (nonbridging) values range from 1.937 to 1.955 Å and 2.170 Å for the bridging oxygen atom in the Si–O–Si–O chain.

We used the computer simulation methods to computationally optimize the *SD*-Li_2PO_2N structure, initializing the calculations with the experimental structural parameters. The computational optimization was performed using both the pwscf [17] and abinit [18] codes. Essentially the same results were obtained with both codes. The total electronic energy of the optimized *SD*-Li_2PO_2N was computed to be 0.1 eV/Li_2PO_2N lower than the total electronic energies of both s_1-Li_2PO_2N and s_2-Li_2PO_2N found in previous computational studies [10]. The fractional atomic coordinates are well represented by the simulation, however, the lattice parameters are systematically underestimated by the LDA exchange-correlation functional as shown in Table 1. The optimized structure is consistent with the X-ray analysis shown in Fig. 1 and is viewed along the **c**-axis in Fig. 2a. Fig. 2b and c show visualizations of the structure along a phosphonitride chain. In Fig. 2b, contours of

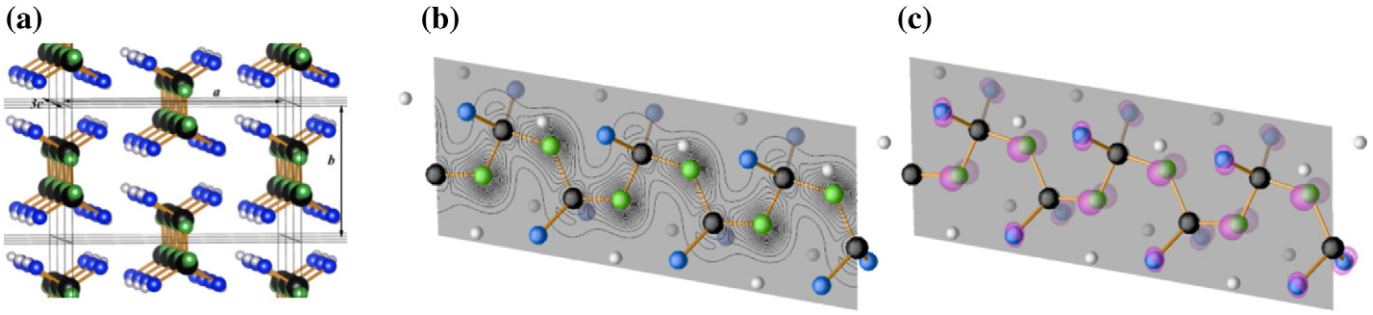

Fig. 2. Ball and stick diagrams of *SD*-Li_2PO_2N using the same sphere color to represent the sites as in Fig. 1. (a) View of crystal along the chains' direction. (b) View of a single chain with a (b–c) crystallographic plane passing through the P–N bonds indicated. Contours representing the valence electron density in this plane are superimposed. (c) View of single chain with superposed plane as shown in (b), with electron density isosurfaces associated with states at the top 1 eV of the valence band indicated in maroon. (For interpretation of the references to color in this figure legend, the reader is referred to the web version of this article.)

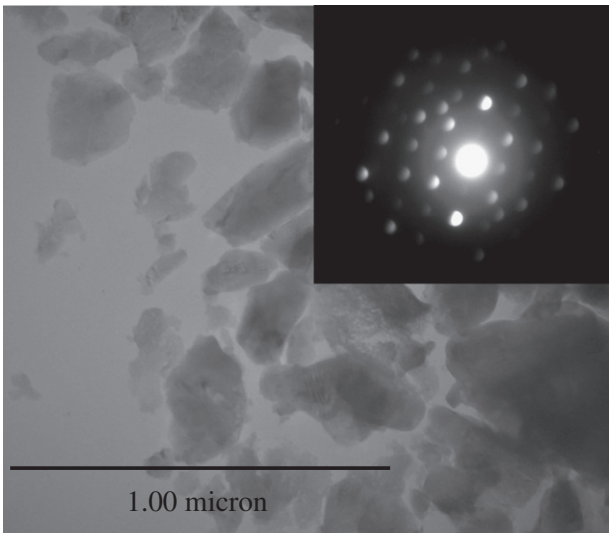

Fig. 3. A representative TEM micrograph and electron diffraction pattern (inset) of *SD*-Li_2PO_2N acquired in bright field mode.

constant electron density are projected onto a b–c plane which passes through the P – N bonds. In Fig. 2c the same viewpoint is presented along with electron density isosurfaces associated with states at the top 1 eV of the valence band indicated. These states have their largest density primarily perpendicular to the plane of the chain consistent with their N 2p π character; a small contribution from the O 2p states is also evident in this plot.

3.3. Morphological analysis by transmission electron microscopy (TEM)

The morphology of *SD*-Li_2PO_2N was investigated using transmission electron microscopy. A representative TEM image is shown in Fig. 3 along with electron diffraction pattern (Fig. 3 inset). The TEM micrograph indicates that *SD*-Li_2PO_2N particles exhibit irregular shape morphology with particle sizes in the micron range. High degree of crystallinity, which has been observed from XRD pattern, is again evidenced by the presence of well resolved diffraction points as seen in the electron diffraction pattern. A summary of d-spacing values calculated from XRD and electron diffraction data is provided in the supporting information (Table S2). The calculated and observed d-spacing values are similar to each other, further strengthening the structural analysis of *SD*-Li_2PO_2N.

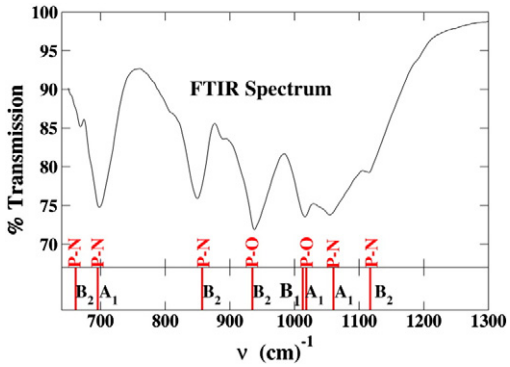

Fig. 5. Measured infrared transmission spectrum (top) compared with calculated zone center lattice infrared active vibration frequencies (bottom). The designated mode symmetry and dominant atomic motions are indicated for each calculated mode.

3.4. Structural and thermal stability of SD-Li_2PO_2N

In order to evaluate the thermal and structural stability of *SD*-Li_2PO_2N, thermogravimetric analysis (TGA) under air and variable temperature XRD measurements under ambient condition and vacuum were performed. There is a prominent weight gain that starts at approximately 600 °C and completes by 900 °C (Fig. 4a). The total percentage weight gain is similar to that of theoretical weight gain (11%) expected if *SD*-Li_2PO_2N undergoes oxidation according to the reaction

$$2Li_2PO_2N(s) + \frac{5}{2}O_2(g) \rightarrow Li_4P_2O_7(s) + 2NO(g).$$

In order to discern the structural changes that occur upon heating, variable temperature XRD was performed. Interestingly, no structural changes were observed upon heating under vacuum even at 1050 °C. However, heating in air changes the structural integrity of *SD*-Li_2PO_2N (Fig. 4b). The XRD patterns clearly indicate that the structure is stable up to 600 °C. Further heating at 700 °C leads to the formation of crystalline $Li_4P_2O_7$, as identified from X-ray analysis [29]. This structural change agrees well with the percent weight gain observed in TGA

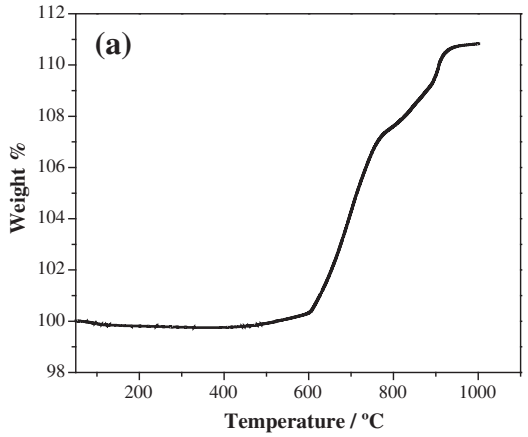

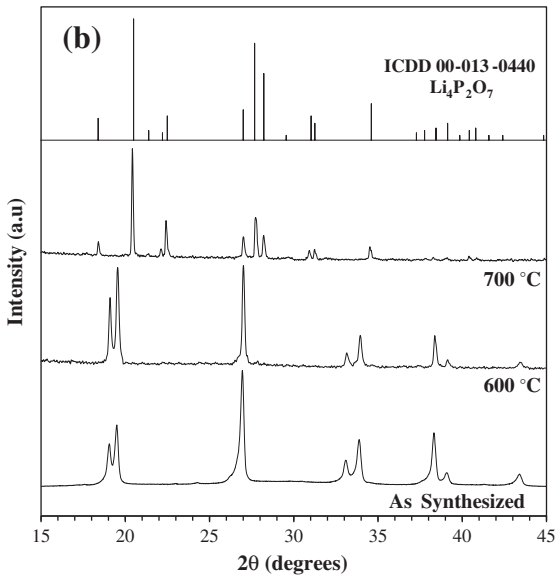

Fig. 4. Plots of (a) TGA curve heated up to 1000 °C in air and (b) XRD patterns of *SD*-Li_2PO_2N heated in air at 600 and 700 °C compared with the room temperature "as synthesized" pattern. The reference XRD pattern of the $Li_4P_2O_7$ decomposition material is shown on the top panel.

Table 2
List of calculated normal mode vibration frequencies in cm^{-1} "Calc" compared with measured infrared transmission peaks "Exp" for *SD*-Li_2PO_2N. Symmetry labels "Sym" are also given. Note that for this crystal vibrational symmetry C_{2v}, most of the modes are both infrared and Raman active, except for the A_2 modes which are only Raman active. The last column lists the calculated mode amplitudes in terms of the sums of the squares of the normal mode vectors for each atom type, normalized to unity.

Calc	Exp	Sym	Mode amplitudes			
			P	N	O	Li
607		B_1	0.09	0.58	0.22	0.11
662	669	B_2	0.20	0.34	0.23	0.23
696	698	A_1	0.12	0.70	0.17	0.01
857	850	B_2	0.33	0.64	0.02	0.01
935	938	B_2	0.12	0.02	0.85	0.00
1011	R only	A_2	0.27	0.00	0.72	0.00
1013 }	1016	B_1	0.27	0.00	0.73	0.00
1018 }		A_1	0.21	0.00	0.78	0.00
1060	1055	A_1	0.08	0.91	0.01	0.00
1117	1115	B_2	0.06	0.93	0.01	0.00

analysis and with the proposed oxidation reaction discussed above. Therefore, we surmise that *SD*-Li_2PO_2N undergoes oxidation to form $Li_4P_2O_7$ above 600 °C.

3.5. Vibrational spectrum

Another measure of the structure is the lattice vibrations. Fig. 5 shows the infrared transmission spectrum measured at room temperature (top) and the calculated infrared active modes (bottom); the symmetry labels and dominant vibrational motions are also indicated. The calculations were done using the pwscf code [17], which uses density functional perturbation theory [30,31] to construct the dynamical matrix for the lattice from which the infrared lattice vibrational modes are determined. The P – N vibrations involve motions primarily in the plane of the chain (b–c), while the P – O modes include motions perpendicular to the chain. In this frequency range, the resonant Li site motions are negligible. In fact, in this frequency range the vibrational spectrum found for *SD*-Li_2PO_2N is similar to that previously reported [10] for s_1-Li_2PO_2N, indicating that these vibrations represent primarily intrachain motions, only weakly depending on the stacking of the chains within the crystal. The general agreement between the measured and calculated vibrational spectrum is impressive and consistent with our experience with previous investigations of Li_3PO_4 [32] and P_3N_5 [10]. In fact, one of the reasons for choosing the LDA exchange-correlation functional [22] for the present study, was its demonstrated ability to reproduce the phonon spectrum in related materials.

Table 2 lists the calculated and measured normal mode vibrational frequencies. Also listed is a measure of the normal mode distribution in terms of the sum of the squares of the amplitudes of the eigenvector for each atom type. The highest frequency modes are P – N vibrations in the crystallographic (b–c) plane, while the P – O vibrations are at slightly lower frequency. The Li contributions to the eigenvectors in this frequency range are very small.

3.6. Electronic structure

The band structure diagram of *SD*-Li_2PO_2N is shown in Fig. 6 with the partial density of states indicated on the right. It is evident from this diagram that the only appreciable dispersion of this material occurs along the c (or G_3) direction as seen in the G–Z and T–Y segments of the band diagram [33]. The states showing appreciable dispersion are associated with the sigma bonds of the P – N chains as visualized in the contour plot diagram shown in Fig. 2b. In contrast, the top of the valence band is essentially flat. The states at the top of the valence band are primarily 2pπ states of N as visualized in the isosurface plot shown in Fig. 2c. Since these states are spatially separated, they form non-dispersive bands. Since density functional theory, particularly using the local density approximation notoriously underestimates the band gap, we can conclude that the band gap of *SD*-Li_2PO_2N is greater than 6 eV, somewhat larger than the predicted band gaps of the s_1 and s_2 structures [10].

It is interesting to note that the pattern of the valence band being very flat, due to well-separated π orbitals, has been previously been reported for Na_2SiO_3 [34,35] and for Li_2SiO_3 [36]. For these materials and their glassy analogs, the terminology – "BO" and "NBO" is used to distinguish between "bridging oxygen" – and "non-bridging oxygen", respectively. For *SD*-Li_2PO_2N, the π bands are due to "bridging nitrogen" rather than "bridging oxygen" and the corresponding electron energy bands are very flat, having a dispersion of less than 0.1 eV.

3.7. Ionic conductivity

The conductivity measured for two *SD*-Li_2PO_2N pellets with a compactness of 55% and 78% of the theoretical density (*i.e.* compactness) is shown in Fig. 7. As expected, conductivity increased with an increase in pellet density. For the 78% dense sample, the conductivity increased from 8.8×10^{-7} S/cm at 80 °C to 1.2×10^{-3} S/cm at 330 °C. One can expect higher conductivity values as the pellet density approaches 100% compactness. While the conductivity increased with compactness, the activation energy remained the same with a value of 0.57 eV.

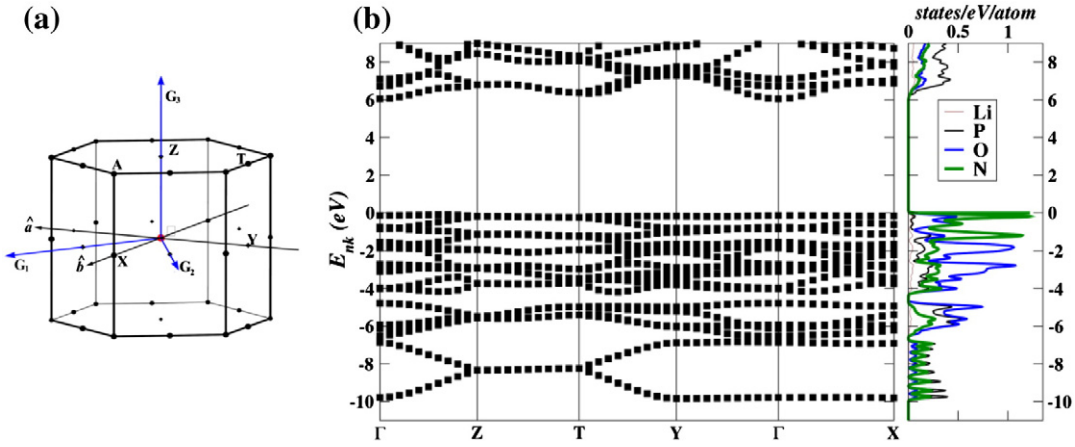

Fig. 6. (a) Brillouin zone diagram for $Cmc2_1$ structure based on labels given by Setyawan [37] drawn to scale by the program Xcrysden. The directions of the a and b axes consistent with conventions of this paper are indicated; the c direction is along the indicated G_3 axis. (b) Valence energy bands and their corresponding partial densities of states of *SD*-Li_2PO_2N. The zero of energy is referenced to the top of the valence band energy. The weighting factor for the partial density of states is the charge density within spheres of radii 1.6, 1.7, 1.2, and 1.2 bohr for the Li, P, O, and N sites, respectively.

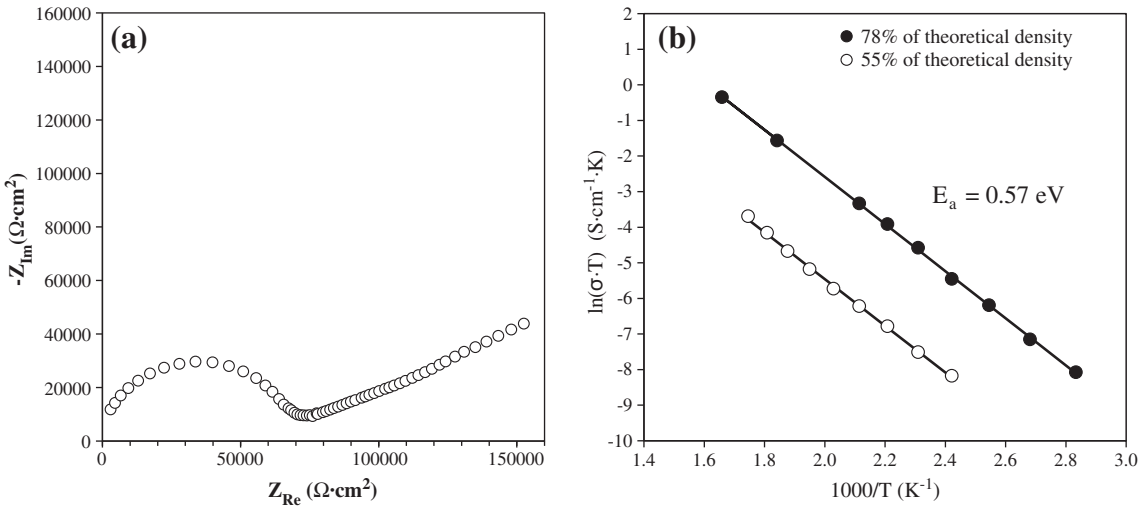

Fig. 7. (a) Real and imaginary impedance measurements for *SD*-Li_2PO_2N at 260°C for a pellet with 55% of the theoretical density. (b) Arrhenius plot of measured impedance for *SD*-Li_2PO_2N for pellets with 55% and 78% of the theoretical density.

We computationally examined vacancy and interstitial Li^+ defects and their migration energies by approximating the crystals with a $1\times2\times2$ supercell. The Li^+ ions occupy only one unique site in the perfect crystal, and consequently Li^+ ion vacancy all have the same geometry and same coordination. On the basis of NEB calculations [38–40] we estimate the migration activation energy for the vacancy mechanism to be $0.4\leq E_m\leq0.6$ eV for hops to near neighbor vacancy sites as illustrated in Fig. 8. The most energetically favorable migration occurs for a zig-zag path along the c-axis between chains, while hopping along the a-axis within a chain or between chains in the a- and b-axes have higher migration energies. The simulation found two types of Li^+ ion interstitial sites between the phosphorus oxy-nitride chains as illustrated in Fig. 9. Examples of type "*I*" sites are shown as A, B, and E in the diagram, while type "*II*" sites are shown as C and D with $E_{II}-E_I=0.2$ eV. The activation energy for migration between neighboring interstitial sites was found to be $0.8\leq E_m\leq0.9$ eV, with hops involving the type *II* sites more energetically favorable than those involving only type *I* sites. This analysis suggests that for this material, the Li^+ ion vacancy migration mechanism is the more energetically favorable.

Li^+ ion conductivity measurements of Li_2PO_2N additionally involve the formation energy E_f to produce a vacancy-interstitial defect pair from the perfect crystal. The simulations find the smallest value

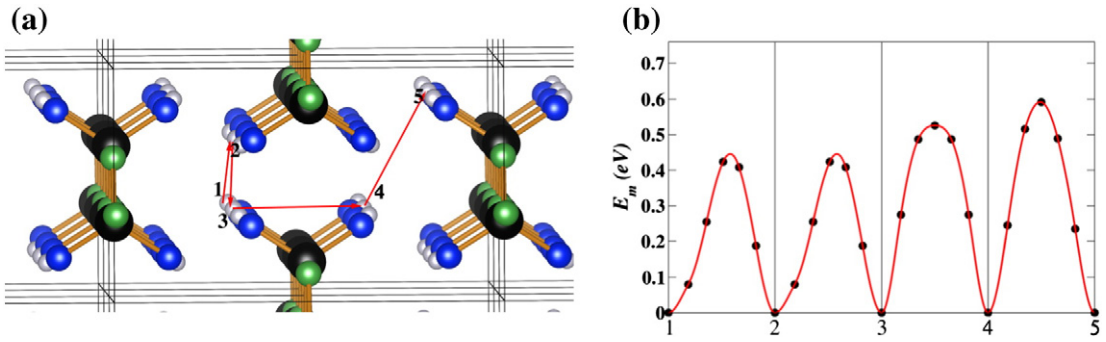

Fig. 8. (a) Ball and stick diagram of possible Li ion vacancy migration path in Li_2PO_2N using same viewpoint shown in Fig. 2a. (b) Migration energy diagram from NEB results for this vacancy mechanism.

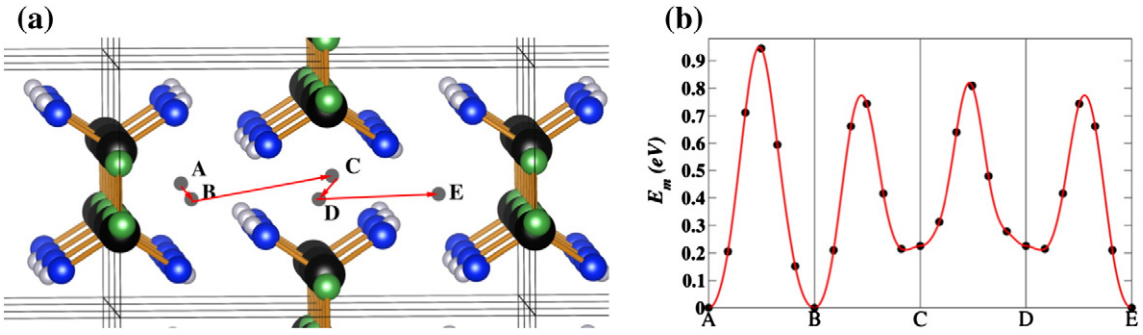

Fig. 9. (a) Ball and stick diagram of possible Li ion interstitial migration path in Li_2PO_2N using same viewpoint shown in Fig. 2a. (b) Migration energy diagram from NEB results for this interstitial mechanism.

to be approximately $E_f = 2$ eV. If this is correct, measurement of the Li^+ ion conductivity would have an activation energy of

$$E_A = E_m + \frac{1}{2}E_f \geq 1.4 \text{ eV}.$$

It is interesting to note that the measured activation energies for Li_2PO_2N are significantly smaller than this; $E_A^{exp} \approx 0.6$ eV presented above is close to the computed vacancy migration energies E_m. One possible explanation is that *SD*-Li_2PO_2N may have a significant number of native defects available for transport so that the thermal production of vacancy-interstitial defect pairs does not control the conductivity. The most important conclusion here is that the measured activation energies for Li_2PO_2N are similar to those reported for amorphous LiPON thin films.

4. Summary and conclusions

LiPON electrolytes developed and used for applications in solid state microbatteries [1] have a disordered glassy form. By contrast the new *SD*-Li_2PO_2N has one of the simplest structures of the LiPON family of materials. The planar P–N–P–N backbone is stabilized by the N 2p π states. The strong bonding structure undoubtedly contributes to the chemical and structural stability of the material up to 1050 °C in vacuum and up to 600 °C in air. The first-principles calculation results are in excellent agreement with experimental structure analysis and with vibrational spectroscopy. The calculations find the *SD*-Li_2PO_2N structure to be more stable by 0.1 eV/Li_2PO_2N than the s_1 and s_2 structures predicted in earlier computational studies [10].

The computed minimum activation energy ($E_A = 1.4$ eV) for Li ion conduction in *SD*-Li_2PO_2N is slightly larger than that of Li_3PO_4 [41], primarily due to the large energy cost (E_f) of producing a vacancy-interstitial defect pair. The computed vacancy and interstitial migration energies E_m are comparable to or lower than those computed for Li_3PO_4 and measured for a variety of LiPON compositions [1]. Interestingly, the measured activation energy for ionic conductivity was found to be $E_A^{exp} = 0.6$ eV which is comparable to the computed vacancy migration energy $E_m = 0.4$–0.6 eV, leading us to speculate that the as-synthesized *SD*-Li_2PO_2N has a significant population of native Li^+ defects.

In future work, we will investigate the full range of properties of *SD*-Li_2PO_2N including a comparison with the iso-structural material Li_2SiO_3.

Acknowledgments

The work was supported by the Wake Forest University Center for Energy, Environment, and Sustainability and by NSF grants DMR-1105485 and MRI-1040264. Computations were performed on the Wake Forest University DEAC cluster, a centrally managed resource with support provided in part by the University. Helpful discussions with R. T. Williams are gratefully acknowledged. Additional experimental help from David Hobart and Brian Hanson from Virginia Tech and Baxter McGuirt from Wake Forest University Center for Nanotechnology and Molecular Materials are also gratefully acknowledged.

Appendix A. Supplementary data

Tables S1, S2, and Crystallographic Information File (CIF) for the final crystal structure solution resulting from the *ab initio* simulated annealing fit for XRD of *SD*-Li_2PO_2N. Supplementary data associated with this article can be found, in the online version, at http://dx.doi.org/10.1016/j.ssi.2012.12.013.

References

[1] N.J. Dudney, Interface 17 (3) (2008) 44–48.
[2] J.B. Bates, N.J. Dudney, B. Neudecker, A. Ueda, C.D. Evans, Solid State Ionics 135 (2000) 33–45.
[3] X. Yu, J.B. Bates, G.E. Jellison, F.X. Hart, J. Electrochem. Soc. 144 (1997) 524–532.
[4] B. Wang, B.C. Chakoumakos, B.C. Sales, B.S. Kwak, J.B. Bates, J. Solid State Chem. 115 (1995) 313–323.
[5] B. Wang, B.S. Kwak, B.C. Sales, J.B. Bates, J. Non-Cryst. Solids 183 (1995) 297–306.
[6] J.B. Bates, N.J. Dudney, D.C. Lubben, G.R. Gruzalski, B.S. Kwak, X. Yu, R.A. Zuhr, J. Power Sources 54 (1995) 58–62.
[7] J.B. Bates, G.R. Gruzalski, N.J. Dudney, C.F. Luck, X. Yu, Solid State Ionics 70–71 (1994) 619–628.
[8] J.B. Bates, N.J. Dudney, G.R. Gruzalski, R.A. Zuhr, A. Choudhury, D.F. Luck, J.D. Robertson, J. Power Sources 43–44 (1993) 103–110.
[9] J.B. Bates, N.J. Dudney, G.R. Gruzalski, R.A. Zuhr, A. Choudhury, C.F. Luck, J.D. Robertson, Solid State Ionics 53–56 (1992) 647–654.
[10] Y.A. Du, N.A.W. Holzwarth, Phys. Rev. B 81 (2010) 184106.
[11] E.V. Murashova, N.N. Chudinova, Crystallogr. Rep. 46 (2001) 942–946.
[12] K.-F. Hesse, Acta Crystallogr. B 33 (1977) 901–902.
[13] Bruker, DIFFRAC.EVA (Version 2.0), Bruker AXS Inc., 5465 East Cheryl Parkway, Madison, WI 53711-5373, 2011.
[14] Bruker, DIFFRAC.TOPAS (Version 4.2), Bruker AXS Inc., 5465 East Cheryl Parkway, Madison, WI 53711-5373, 2009.
[15] P. Hohenberg, W. Kohn, Phys. Rev. 136 (1964) B864–B871.
[16] W. Kohn, L.J. Sham, Phys. Rev. 140 (1965) A1133–A1138.
[17] P. Giannozzi, S. Baroni, N. Bonini, M. Calandra, R. Car, J. Phys. Condens. Matter 21 (2009) 395502.
[18] X. Gonze, B. Amadon, P.-M. Anglade, J.-M. Beuken, Comput. Phys. Commun. 180 (2009) 2582–2615.
[19] A.R. Tackett, N.A.W. Holzwarth, G.E. Matthews, Comput. Phys. Commun. 134 (2001) 348–376.
[20] P.E. Blöchl, Phys. Rev. B 50 (1994) 17953–17979.
[21] N.A.W. Holzwarth, A.R. Tackett, G.E. Matthews, Comput. Phys. Commun. 135 (2001) 329–347.
[22] J.P. Perdew, B. Wang, Phys. Rev. B 45 (1992) 13244–13249.
[23] OpenDX — an open source software project based on IBM's Visualization Data Explorer; available from the website http://www.opendx.org.
[24] A. Kokalji, J. Mol. Graph. Model. 17 (1999) 176–179.
[25] K. Momma, F. Izumi, J. Appl. Crystallogr. 44 (2011) 1272–1276.
[26] H.J. Monkhorst, J.D. Pack, Phys. Rev. B 13 (1976) 5188–5192.
[27] T. Hahn, International Tables for Crystallography, Volume A: Space-group Symmetry, 5th edition, Kluwer, 2002.
[28] F.H. Allen, Acta Crystallogr. B 58 (2002) 380–388.
[29] ICDD, Powder Diffraction File PDF-2 I, 2011. (12 Campus Blvd., Newtown Square, PA 19073 USA).
[30] C. Audouze, F. Jollet, M. Torrent, X. Gonze, Phys. Rev. B 78 (2008) 035105.
[31] A. Dal Corso, Phys. Rev. B 81 (2010) 075123.
[32] Y.A. Du, N.A.W. Holzwarth, Phys. Rev. B 76 (2007) 174302.
[33] Note that the spikey appearance of the density of states plot in the energy range $-10 < Enk < 7.5$ eV is an artifact of the Brillouin zone sampling.
[34] W.Y. Ching, R.A. Murray, J., L. D., B.W. Veal, Phys. Rev. B 28 (1983) 4724–4735.
[35] F. Liu, S.H. Garofalini, R.D. King-Smith, D. Vanderbilt, Chem. Phys. Lett. 215 (1993) 401–404.
[36] T. Tang, P. Chen, W. Luo, D. Luo, Y. Wang, J. Nucl. Mater. 420 (2012) 31–38.
[37] W. Setyawan, S. Curtarolo, Comput. Mater. Sci. 49 (2010) 299–312.
[38] H. Jónsson, G. Mills, K.W. Jacobson, in: B.J. Berne, G. Ciccotti, D.F. Coker (Eds.), Classical and Quantum Dynamics in Condensed Phase Simulations, World Scientific, Singapore, 1998, pp. 385–404.
[39] G. Henkelman, B.P. Uberuaga, H. Jónsson, J. Chem. Phys. 113 (2000) 9901–9904.
[40] G. Henkelman, H. Jónsson, J. Chem. Phys. 113 (2000) 9978–9985.
[41] A.K. Ivanov-Shitz, V.V. Kireev, O.K. Mel'nikov, L.N. Demainets, Crystallogr. Rep. 46 (2001) 864–867.